Global NEST Journal, **28** (7), 08607
Available online: 01/10/2026

Optimization of Rice Husk Biochar-Modified Nickel Tailings Coupled with *Bacillus cereus* for Cr(VI) Remediation in Simulated Groundwater

Qiyang Wang[1], Yunfei Li[1], Yuan Zhao[1], Meitang Liu[1]*, Yexin Zhang[1], Haixin Hou[1], Xin Huang[2], Guangjie Zhang[3]

[1]Materials Department, School of Materials Science and Engineering, China University of Geosciences (Beijing), P. R. China
[2]Information Management and Information System Department, School of Economics and Management, China University of Geosciences (Beijing), P. R. China
[3]Information Measurement Department, Control Technology and Instrumentation, School of Geophysics and Information Technology, China University of Geosciences (Beijing), P. R. China

*Correspondence e-mail: mtliu@cugb.edu.cn

Abstract

Hexavalent chromium (Cr(VI)) is a toxic heavy metal pollutant posing severe risks to ecosystems and human health. Herein, a modified nickel tailings–rice husk biochar composite (MNR) was fabricated via co-pyrolysis of nickel tailings and rice husk powder and coupled with *Bacillus cereus* to construct a Cr(VI)-contaminated groundwater remediation system. Under optimized conditions, 99.81% ± 0.06% of Cr(VI) was removed within 18 h from simulated groundwater with an initial Cr(VI) concentration of 50 mg L^{-1}. The highly toxic and mobile exchangeable Cr(VI) was reduced to less toxic Cr(III), which was further immobilized as solid-phase hydroxide precipitates, enabling stable chromium sequestration in the aqueous system. This work provides an alternative strategy for Cr(VI)-contaminated groundwater remediation, with advantages of high removal efficiency and waste valorization of industrial and agricultural solid wastes.

Keywords: nickel tailings, *Bacillus cereus*, biochar, solid waste utilization, hexavalent chromium remediation.

OPEN ACCESS

Received: 28/02/2026,

Accepted: 29/09/2026,

Available online: 01/10/2026

Copyright: © 2026 The Author(s). Published in Global NEST Journal. This article is licensed under the terms and conditions of the Creative Commons Attribution 4.0 International license (CC BY 4.0).

Graphical abstract

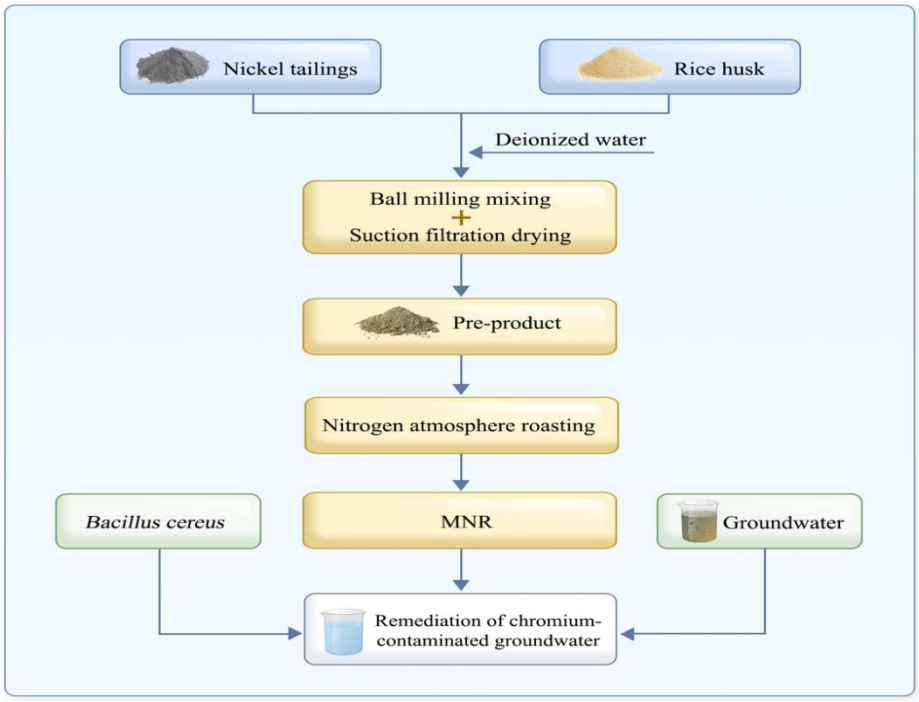

1. Introduction

Rapid industrialization and urbanization have aggravated heavy metal contamination in global soil and aquatic environments. Hexavalent chromium (Cr(VI)) is a ubiquitous pollutant with high aqueous solubility, environmental persistence and poor biodegradability (Jiang *et al.*, 2026). Classified as a Group 1 human carcinogen by the International Agency for Research on Cancer (IARC) (Tripathi *et al.*, 2024), it poses severe threats to ecosystems and public health due to its extreme toxicity and high mobility. Waterborne Cr(VI) mainly originates from industrial wastewater discharges from electroplating, leather tanning, textile dyeing and stainless steel manufacturing (Irshad *et al.*, 2023), and poses cumulative health risks even at trace concentrations (Liu *et al.*, 2023; Manoj *et al.*, 2020).

Developing efficient Cr(VI) remediation technologies remains a high-priority research need. Three interrelated but distinct performance metrics are clarified: Cr(VI) reduction denotes the valence conversion of Cr(VI) to less toxic Cr(III); Cr(VI) removal refers to the disappearance of dissolved Cr(VI) from the aqueous phase via both reduction and direct adsorption; chromium immobilization is the stable sequestration of total chromium in the solid phase, serving as the ultimate goal of remediation. Conventional Cr(VI) treatment technologies include chemical precipitation, ion exchange, membrane filtration and adsorption. Among them, adsorption has attracted extensive attention for its operational simplicity, cost-effectiveness and robust performance (Sinha *et al.*, 2022).

As a representative carbonaceous adsorbent, biochar shows considerable promise for aqueous Cr(VI) remediation, benefiting from its large specific surface area, well-developed hierarchical porous structure and abundant surface functional groups (Sinha *et al.*, 2022; Yang *et al.*, 2024). However, pristine biochar exhibits limited Cr(VI) adsorption and reduction capacities, which constrains its overall Cr(VI) removal efficiency (Li *et al.*, 2024; Liu *et al.*, 2025). Although modified biochar composites can improve performance to some extent, their potential secondary pollution risks contradict the core principle of sustainable biochar-based remediation. Accordingly, there remains an urgent need to develop alternative modification strategies to improve the practical applicability of biochar.

Coupling biochar with functional microorganisms is a widely used water remediation strategy, effective for removing heavy metals, organic pollutants and ammonia nitrogen. Chen *et al.* (2019) fabricated biochar–microbe composites using rice husk and sludge biochar as carriers to immobilize phosphate-solubilizing bacteria via adsorption, and tested their Pb(II) removal performance in wastewater. Compared with pristine biochar systems, the composites increased Pb(II) removal efficiency from 18.61% to 24.11% (rice husk biochar group) and from 53.89% to 60.85% (sludge biochar group), verifying the synergistic enhancement effect. Building on this, coupling functional biochar composites with Cr(VI)-reducing microorganisms holds strong potential for integrating interfacial chromium retention and sustained

biotransformation, improving both Cr(VI) removal and long-term immobilization.

Iron-based materials, typically nanoscale zero-valent iron (nZVI), are widely applied for biochar modification to enhance Cr(VI) removal efficiency owing to their strong reducing capacity (Mondal *et al.*, 2025; Li *et al.*, 2025). During reactions, Fe(0) in nZVI reduces Cr(VI) to Cr(III) while being oxidized to Fe(II) and Fe(III) species (Hou *et al.*, 2025). However, nZVI suffers from gradual reductive capacity depletion and surface passivation caused by iron hydroxide precipitates during long-term operation, limiting its sustained reactivity. As a porous support, biochar effectively inhibits nZVI aggregation and oxidation while providing abundant surface active sites for pollutant binding (Xiong *et al.*, 2025). For instance, Cheng *et al.* (2024) synthesized corn stalk biochar-supported sulfidated nZVI (S-nZVI@BC), which achieved rapid Cr(VI) removal from aqueous solutions with excellent dispersibility and transport stability. Qiao *et al.* (2025) reported that carboxymethyl cellulose-stabilized biochar-supported nZVI (CMC-nZVI@BC) attained 99.9% Cr(VI) removal within 180 min, 22.4% higher than pristine nZVI@BC. Additionally, iron-modified straw biochar prepared via a precipitation–pyrolysis route enables valorization of waste biomass into functional Cr(VI) removal materials (Liu *et al.*, 2025).

To date, few studies have explored the synergistic potential of multi-metal components from industrial solid wastes such as nickel tailings. Notably, nickel tailings are dominated by iron oxides and other associated mineral components with negligible metallic nickel content. Systematic research on biochar coupled with multi-metal waste fractions for Cr(VI) remediation remains scarce, leaving a clear research gap.

This work addresses two interconnected environmental challenges: widespread aqueous Cr(VI) contamination and sustainable valorization of industrial and agricultural solid wastes. A multifunctional nickel tailings–rice husk biochar composite (MNR) with both reductive activity and microbial carrier functions was fabricated via co-calcination of rice husk and nickel tailings, and coupled with *Bacillus cereus* to enhance aqueous Cr(VI) removal. The effects of raw material ratio, calcination parameters, material–microbe synergy and reaction time on Cr(VI) removal efficiency were systematically investigated. This strategy achieves simultaneous valorization of agricultural and industrial solid wastes through the synergistic effect of enhanced interfacial chromium retention by MNR and microbial Cr(VI) reductive transformation. Under optimized conditions, the MNR–*Bacillus cereus* system achieved 99.81% ± 0.06% Cr(VI) removal within 18 h from simulated groundwater with an initial Cr(VI) concentration of 50 $mg \cdot L^{-1}$. Compared with reported biochar–microbe systems, which typically yield only 5%–10% heavy metal removal enhancement over pristine biochar (Chen *et al.*, 2019), this system exhibits a significantly stronger synergistic effect, providing a promising alternative for sustainable aqueous Cr(VI) remediation.

2. Experimental section

2.1. *Materials*

Nickel tailings, a typical industrial solid waste generated from nickel ore beneficiation and smelting, were obtained from Jinchuan Group Co., Ltd. (Jinchuan, Gansu Province, China). The elemental composition of the raw nickel tailings was determined via inductively coupled plasma optical emission spectrometry (ICP-OES) (Agilent 5110, Agilent Technologies, Santa Clara, CA, USA) after complete acid digestion. The corresponding compositional results are presented in **Table 1**.

Table 1. Elemental composition of the raw nickel tailings feedstock.

SiO_2	TiO_2	Al_2O_3	Fe_2O_3	MnO	MgO	CaO	Na_2O	K_2O	P_2O_5	LOI	Total
36.29	0.23	3.17	17.85	0.13	28.09	2.31	0.38	0.29	0.06	10.59	99.39

Rice husk powder was prepared by grinding rice husks harvested from farmland in Lianyungang, Jiangsu, China. *Bacillus cereus* (strain CGMCC 1.3760, equivalent to the type strain ATCC 14579) was purchased from a certified commercial microbial strain supplier in Beihai, Guangxi, China. Strain identity was verified via 16S ribosomal RNA (16S rRNA) gene Sanger sequencing. The sequence was aligned against the NCBI GenBank database via Basic Local Alignment Search Tool (BLAST), showing 99.2% similarity to the reference *Bacillus cereus* ATCC 14579 sequence (GenBank accession no. AF290547.1). This strain mediates Fe(II)/Fe(III) redox cycling under trace iron conditions via environmental electron mediators, and the generated reducing equivalents can drive reduction of multiple elemental species (Xiang *et al.*, 2024). It was employed herein as the core functional microorganism for Cr(VI) reduction to Cr(III). Other reagents: sulfuric acid (H_2SO_4, 98%, Sinopharm), phosphoric acid (H_3PO_4, 70%, Sinopharm), acetone (99%, Macklin), 1,5-diphenylcarbazide (DPC, 99%, Sinopharm), chromium standard stock solution (100.0 mg/L, Macklin), sodium hydroxide (NaOH, 99%, Aladdin), potassium chloride (KCl, 99%, Aladdin), ammonium chloride (NH_4Cl, 99%, Aladdin), sodium chloride (NaCl, 99%, Aladdin), calcium chloride ($CaCl_2$, 99%, Aladdin), magnesium chloride ($MgCl_2$, 99%, Aladdin), magnesium chloride hexahydrate ($MgCl_2 \cdot 6H_2O$, 99%, Aladdin), potassium dihydrogen phosphate (KH_2PO_4, 99%, Aladdin), sodium bicarbonate ($NaHCO_3$, 99%, Aladdin), potassium dichromate ($K_2Cr_2O_7$, 99%, Aladdin), tryptone (Aladdin), and yeast extract (40%, Aladdin). All reagents were analytical grade and produced in China.

2.2. *Design of experiment*

2.2.1. Simulated groundwater

Simulated groundwater was prepared with laboratory reagents, containing KCl (28.3 $mg \cdot L^{-1}$), NH_4Cl (155.7 $mg \cdot L^{-1}$), NaCl (455.9 $mg \cdot L^{-1}$), $CaCl_2$ (246.4 $mg \cdot L^{-1}$), magnesium chloride hexahydrate (1057.2 $mg \cdot L^{-1}$), potassium

dihydrogen phosphate (29.9 mg·L^{-1}), sodium bicarbonate (808.2 mg·L^{-1}), and other trace components. Cr(VI)-spiked synthetic groundwater was prepared by adding $K_2Cr_2O_7$ to the synthetic groundwater matrix, yielding an initial Cr(VI) concentration of 50.0 mg·L^{-1}.

2.2.2. Nickel tailings modification

Nickel tailings and rice husk powder were separately ball-milled, sieved through a 50-mesh sieve, and mixed at preset mass ratios (gradients detailed in Section 2.3). Deionized water was added to the mixture, and the suspension was stirred at 240 rpm for 2 h with a constant-speed electric stirrer, then separated by vacuum filtration. The collected solids were rinsed, air-dried in a cool well-ventilated area, re-ball-milled, and sieved through a 100-mesh sieve. The pretreated powders were calcined in corundum crucibles in a nitrogen-atmosphere tube furnace for 2 h isothermally (temperature gradients detailed in Section 2.3). The final products were designated as MNR composites.

2.2.3. Expansion culture of Bacillus cereus

Bacillus cereus was expanded in Luria–Bertani (LB) medium (pH 6.5–7.5), dispensed into Erlenmeyer flasks, and incubated at 37°C and 160 rpm in a thermostatic shaking incubator (model THZ-98AB; Shanghai Yiheng Scientific Instrument Co., Ltd., China) (Shi *et al.*, 2026; Wang *et al.*, 2023; Lu *et al.*, 2015). Subculturing was performed every 12 h to prepare bacterial suspensions with gradient concentrations. Cell density was quantified by optical density at 600 nm (OD_{600}) (Meyers *et al.*, 2018). All suspensions were freshly subcultured immediately before use, with no significant viability loss observed during preparation.

2.2.4. Cr(VI) remediation experiment

Batch experiments were performed to evaluate Cr(VI) removal performance of the MNR–*Bacillus cereus* system in simulated groundwater. MNR material was added to mixed solutions of Cr(VI)-spiked simulated groundwater and bacterial suspension, and incubated at 37°C and 160 rpm in a thermostatic shaking incubator (THZ-98AB; Shanghai Yiheng Scientific Instrument Co., Ltd.), consistent with bacterial culture conditions.

Samples were collected at 0, 6, 12, 18, 24, 30 and 36 h to monitor aqueous Cr(VI) concentration kinetics. All samples were filtered through disposable microporous membranes before analysis. Experimental group configurations are detailed in Section 2.3. Residual dissolved Cr(VI) was quantified at 540 nm via ultraviolet-visible (UV-Vis) spectrophotometry (UV2200; Beifen Ruili, China) using the DPC method according to standard HG/T 3696.2. Total chromium retained on spent MNR was determined by ICP-OES (Agilent 5110, Agilent Technologies, USA) after acid digestion, to characterize chromium transformation and solid-phase immobilization.

2.2.5. Post-reaction characterization

After Cr(VI) remediation tests, solid and aqueous phases were separated for chromium speciation analysis and immobilization pathway verification. Aqueous Cr(VI) was directly determined by the DPC spectrophotometric method (Section 2.2.4), and dissolved Cr(III) in the final supernatant was quantified by titration. For solid-phase analysis, spent MNR composites were collected by vacuum filtration, rinsed three times with ultrapure water, and dried at 60°C under anoxic conditions to prevent chromium valence transformation. Total chromium retained on the solid matrix was quantified by ICP-OES after complete acid digestion (same procedure as Section 2.2.4).

Solid-phase Cr(VI) was determined by anoxic acid extraction followed by ferrous ammonium sulfate (FAS) titration. Briefly, dried spent MNR was digested with non-oxidizing sulfuric acid in a nitrogen-sealed vessel to avoid Cr(III) oxidation. The leachate was titrated with standard FAS titrant using N-phenylanthranilic acid as redox indicator; the end point was identified by a color shift from purplish-red to light green, and Cr(VI) concentration was calculated from titrant consumption. For total chromium in the leachate, excess ammonium persulfate was added to oxidize all Cr(III) to Cr(VI) prior to titration, and Cr(III) content was derived from the difference between total chromium and Cr(VI). Solid-phase Cr(III) was calculated as the difference between total solid-phase Cr and solid-phase Cr(VI), achieving quantitative valence differentiation.

The FAS titration method was validated before sample testing. The FAS titrant was calibrated with 0.5–20 mg L^{-1} standard Cr(VI) solutions before each batch, with a method detection limit of 0.05 mg L^{-1} for Cr(VI). Spike recovery tests at three concentration levels (1, 5, and 10 mg L^{-1}) yielded recovery rates of 97.26% ± 0.02% to 102.74% ± 0.02%, confirming the accuracy and reliability of the method.

In addition, X-ray photoelectron spectroscopy (XPS) (ESCALAB 250Xi, Thermo Fisher, USA) was performed on spent MNR to characterize surface elemental composition and chromium chemical states. Survey spectra were collected over a binding energy range of 0–1300 eV, and high-resolution Cr 2p spectra were acquired for chromium speciation identification.

2.3. *Comparative experiments*

2.3.1. Standard experimental conditions

Baseline experimental parameters were determined prior to the formal batch tests. Each reaction system had a total liquid volume of 200 mL, consisting of 150 mL of Cr(VI)-spiked simulated groundwater and 50 mL of *Bacillus cereus* suspension. The *Bacillus cereus* suspension was prepared with an inoculation volume fraction of 2% (v/v). The dosage of 600°C-calcined MNR composite was 1 g per system, and the nickel tailings-to-rice husk mass ratio was 1:2. For every test group, an initial sample was collected immediately after bacterial inoculation to record baseline readings, and these baseline data were excluded from subsequent analysis. Subsequent sampling was conducted at 6-h intervals.

2.3.2. Sampling Procedure

Samples were collected by extracting 1 mL of liquid with a sterile syringe from each reaction vessel. The collected

liquid was filtered to separate solid particles, and the filtrate was stored at 4°C in a refrigerator prior to Cr(VI) concentration testing.

2.3.3. Analytical Method

Filtrate Cr(VI) concentrations were measured using the DPC spectrophotometric method following standard HG/T 3696.2.

2.3.4. Experimental and control group design

Test groups covered two nickel-tailings-to-rice-husk mass ratios (1:1 and 1:2) and five calcination temperatures (300°C, 400°C, 500°C, 600°C, and 700°C) to optimize material preparation parameters. For Cr(VI) treatment assays, MNR dosages were set to 0 g, 0.5 g, 1 g, and 2 g, and the volume-based inoculation ratios of *Bacillus cereus* suspension were adjusted to 0% (v/v), 1% (v/v), 2% (v/v), and 5% (v/v) (Gu *et al.*, 2023).

In addition to the gradient test groups, the following control groups were set up to quantify individual contributions and clarify the synergistic mechanism:

(1) **Raw material control groups**: pure nickel tailings group and pure rice husk biochar group, to evaluate the baseline Cr(VI) removal capacity of individual raw feedstocks;
(2) **Single modified material group (MNR alone)**: to quantify the chromium retention capacity of the modified composite independent of microorganisms;
(3) **Single microorganism group (*Bacillus cereus* alone)**:to determine the independent Cr(VI) reduction contribution of the strain;
(4) **Abiotic control groups**: heat-inactivated *Bacillus cereus* group and blank group (neither material nor bacteria), to exclude the interference of medium components and abiotic factors on chromium concentration determination.

All experiments were performed in triplicate under consistent temperature and shaking conditions.

3. Results

3.1. *Surface pore structure and specific surface area of pristine and modified samples*

Figure 1 shows the N_2 adsorption-desorption isotherms of raw rice-husk biochar and the as-synthesized MNR composite. After modification, the specific surface area increases from 2.299 m²/g (raw biochar) to 62.046 m²/g (MNR), total pore volume rises from 0.0098 cm³/g to 0.0562 cm³/g, and average pore diameter decreases from 24.4 nm to 19.3 nm. According to International Union of Pure and Applied Chemistry (IUPAC) criteria, the MNR isotherm is Type IV with a typical H2-type hysteresis loop (Lin *et al.*, 2023), corresponding to slit-shaped or ink-bottle pore geometries. The Barrett-Joyner-Halenda (BJH) pore size distribution spans 0–40 nm. Both materials exhibit hierarchical micro-mesoporous features, with pore size maxima below 2 nm and average pore diameters in the mesoporous range (2–50 nm).

The 30-fold increase in specific surface area and optimized pore structure provide structural support for the remediation process: they facilitate interfacial enrichment of Cr(VI) and offer abundant reaction sites for subsequent reduction, as well as physical confinement for Cr(III)-bearing precipitates, consistent with the proposed immobilization mechanism (Prajapati *et al.*, 2026).

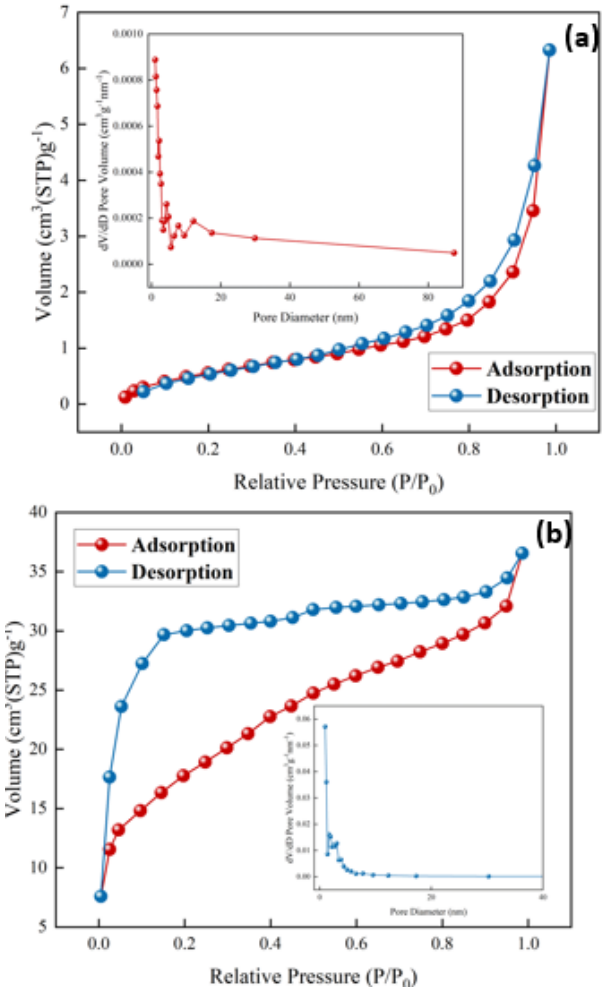

Figure 1. N_2 adsorption-desorption isotherms of raw rice-husk biochar (a) and MNR composite (b).

3.2. *Surface functional groups of pristine and modified samples*

Figure 2 presents Fourier transform infrared (FTIR) spectra of the unpyrolyzed precursor and calcined MNR composite, illustrating changes in surface functional groups induced by high-temperature treatment. For the precursor, absorption peaks at 3686.85, 3431.28, 2920.35, 1637.39, 1017.32 and 610.66 cm⁻¹ are assigned to free Mg–OH stretching, associated hydroxyl (–OH) groups, aliphatic C–H stretching, aromatic C=C stretching, Si–O stretching, and Mg–OH bending, respectively.

After pyrolysis, the aliphatic C–H peak at 2920.35 cm⁻¹ disappears, attributable to organic matter decomposition and carbon aromatization, whereas the aromatic C=C peak is preserved. This spectral feature is consistent with the formation of a carbonized aromatic framework, as reported previously (Xu *et al.*, 2022). The Si–O stretching peak shifts to 1055.86 cm⁻¹ with enhanced intensity, indicating structural rearrangement of silicate components upon calcination.

Notably, both free Mg–OH stretching and bending peaks are absent in the calcined MNR spectrum, suggesting

cleavage of Mg–OH bonds and decomposition of magnesium hydroxide during pyrolysis. The broad absorption band of matrix –OH groups remains distinct with only slight narrowing, indicating that most hydroxyl groups on the biochar matrix are preserved after calcination. Variations in hydroxyl-related signals are primarily attributed to the decomposition of Mg-bearing components rather than extensive dehydration of the biochar skeleton.

MgO formed during calcination may dissolve and release Mg(II) in aqueous environments, potentially participating in chromium redox transformation and hydroxide co-precipitation. Coupled with the surface reactive sites provided by the silicate framework, Mg-derived species and Si–O functional groups likely contribute to chromium transformation and solid-phase retention in the reaction system.

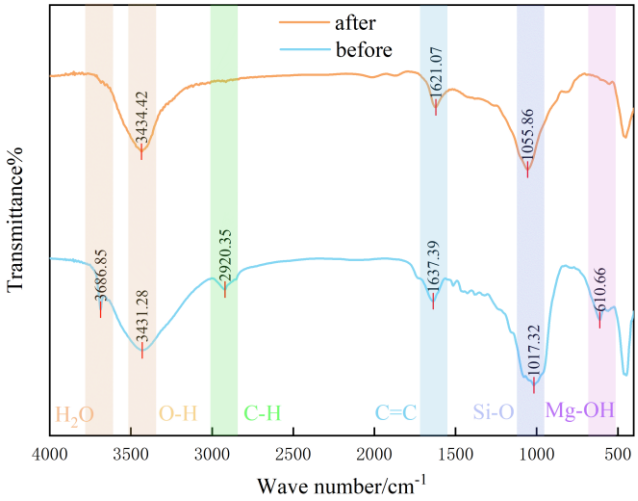

Figure 2. FTIR spectra of the composite system before and after roasting.

3.3. *Component changes in the samples before and after modification*

X-ray diffraction (XRD) tests were conducted on the uncalcined raw sample and samples calcined at 300°C and 600°C. Diffraction patterns were collected using Cu-Kα radiation (λ = 1.5418 Å) within a 2θ scanning range of 10°–80°.

Figure 3 presents XRD patterns of nickel tailings treated under different calcination temperatures. The uncalcined raw sample shows dominant diffraction signals corresponding to the lizardite mineral phase. For the sample calcined at 300°C, new diffraction peaks assignable to hematite are observed (Rowe *et al.*, 2012), likely related to phase transformation of free iron-containing components in raw tailings. Meanwhile, weakened lizardite diffraction peak intensity suggests a decreased relative content of lizardite after low-temperature calcination. After calcination at 600°C, the characteristic peaks of lizardite are no longer detectable, while new diffraction signals corresponding to forsterite appear. This spectral evolution is consistent with the dehydroxylation and decomposition of lizardite to form forsterite under high-temperature conditions, as reported in previous studies (Trittschack *et al.*, 2012). In addition, hematite-related diffraction peaks disappear in the 600°C-calcined sample, indicating possible phase transformation of initial hematite components during calcination. This change may be attributed to the reduction of Fe(III) to Fe(II) species at high temperatures (Zhang *et al.*, 2022). It should be noted that XRD only detects crystalline phases, and weakly crystalline or amorphous phases cannot be identified; the above phase assignments are plausible interpretations based on standard diffraction data.

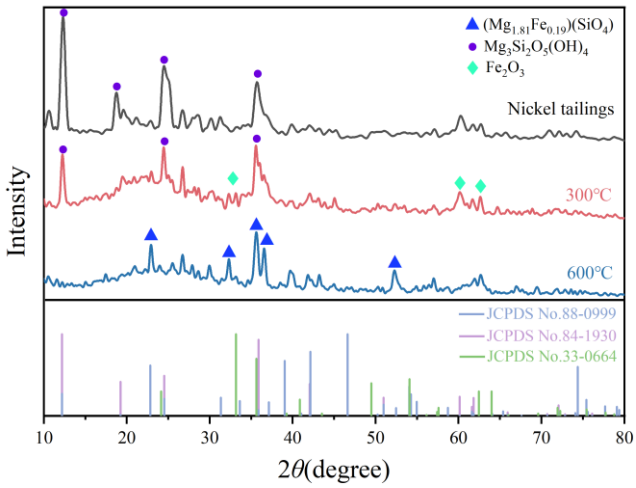

Figure 3. XRD patterns of raw nickel tailings and nickel tailings roasted at 300°C and 600°C.

3.4. *Changes in the chemical states and relative contents of chemical bonds of elements in the samples*

XPS was performed on the uncalcined precursor and 600°C-calcined MNR to investigate the effect of calcination on the chemical states and bonding environments of major elements (Greczynski *et al.*, 2020).

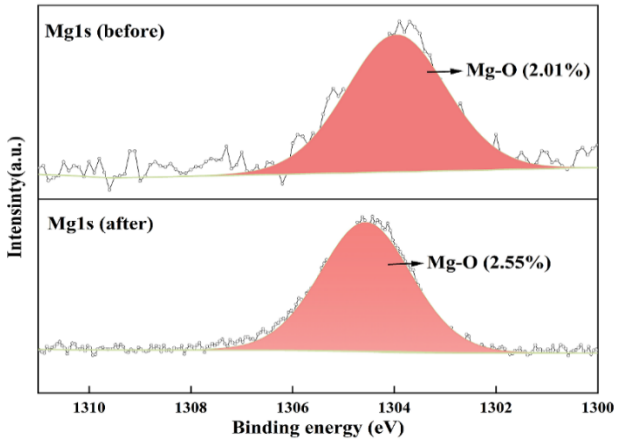

Figure 4. XPS spectra of Mg–O bonds in samples before and after 600°C roasting.

To complement the XRD observations regarding lizardite attenuation and forsterite formation, the relative content of Mg-O bonds in the uncalcined sample and 600°C-calcined sample was analyzed. **Figure 4** shows that the relative proportion of Mg-O bonds increases from 2.01% in the raw sample to 2.55% after calcination at 600°C. Combined with the XRD spectral changes, this variation is consistent with the dehydroxylation and decomposition of lizardite, which may promote forsterite generation under high-temperature conditions (Trittschack *et al.*, 2012). In addition, the spectral results imply that silicate-bound

magnesium species may transform into free MgO during calcination (Radfarnia *et al.*, 2025), and further convert into forsterite at elevated temperatures (Yang *et al.*, 2022).

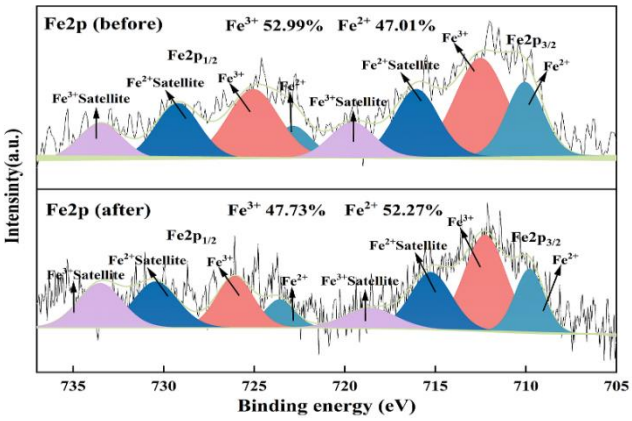

Figure 5. XPS spectra of iron species with different valence states in samples before and after 600°C roasting.

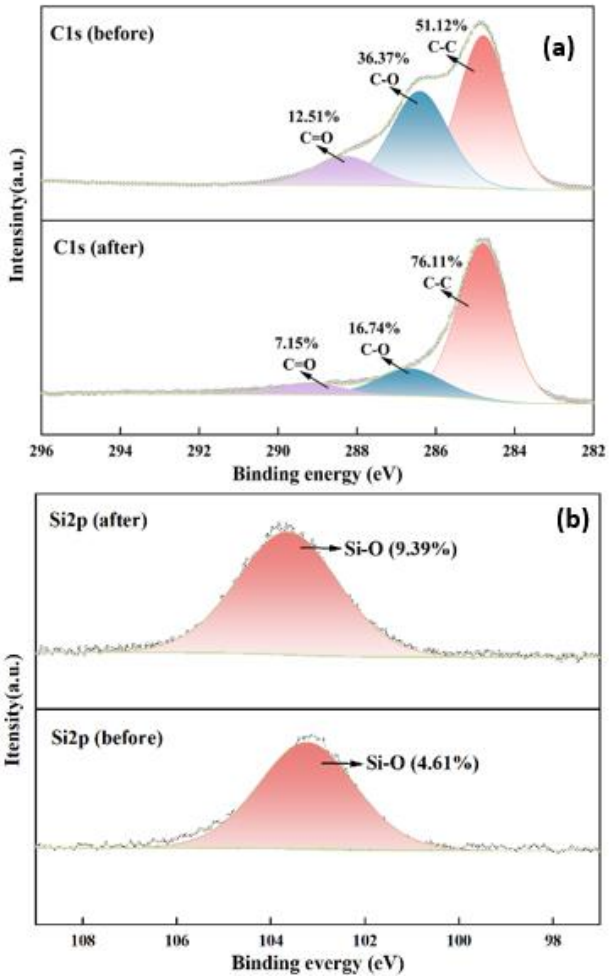

Figure 6. XPS spectra of (a) carbon-containing bonds and (b) Si–O bonds in samples before and after 600°C roasting.

High-resolution Fe 2p spectra (**Figure 5**) reveal a distinct valence shift: the relative proportion of Fe(II) increases from 47.01% in the raw sample to 52.27% after 600°C calcination, while Fe(III) decreases from 52.99% to 47.73%. This indicates partial Fe(III) is reduced to reductive Fe(II) sites during high-temperature calcination, which explains the disappearance of hematite diffraction peaks in the XRD patterns. These Fe(II) sites act as electron donors to drive Cr(VI) reduction to Cr(III), forming the core of the reductive remediation mechanism.

Figure 6(a) and **6**(b) illustrate variations in carbon-related functional groups before and after 600°C calcination. After high-temperature treatment, the relative proportion of C–C bonds increases from 51.12% (uncalcined raw material) to 76.11%. By contrast, the relative contents of C=O and C–O bonds decrease from 12.51% to 7.15% and from 36.37% to 16.74%, respectively. Additionally, the relative proportion of Si–O bonds increases, while the absolute content of silicon-containing components remains stable. These spectral variations may be associated with the pyrolysis of rice husk-derived lignin during 600°C calcination. The carbonization process may transform partial carbon in oxygen-containing functional groups into elemental carbon, corresponding to the increased C–C bond proportion. Lignin pyrolysis is accompanied by dehydration, dehydroxylation and demethoxylation reactions, which may reduce the abundance of C=O and C–O functional groups. Furthermore, volatile gas release during pyrolysis reduces overall sample mass (Wu *et al.*, 2018), which may contribute to the elevated relative proportion of Si–O bonds despite unchanged absolute silicon-based component content.

Figure 7 displays the XPS survey spectra of the uncalcined raw sample and 600°C-calcined sample. After calcination, photoelectron peak intensities of Mg, C and Si increase, O peak intensity declines, and Fe peak intensity remains nearly unchanged. These elemental spectral variations align with the above characterization results, reflecting consistent structural and compositional changes after high-temperature modification.

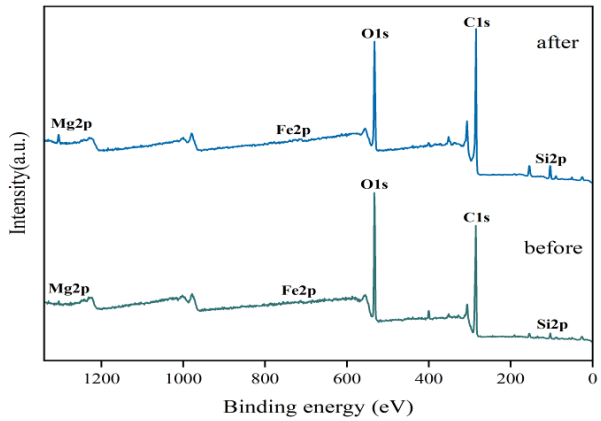

Figure 7. XPS survey spectra of target elements in the raw sample and 600°C-calcined sample.

3.5. *Scanning Electron Microscopy Analysis*

Figure 8(a–f) shows scanning electron microscopy (SEM) micrographs of various samples, revealing microstructural evolution during calcination and its correlation with Cr(VI) remediation performance.

Figure 8(a) shows that raw nickel tailings exhibit an irregular block-stacked morphology with dense, smooth surfaces and limited pore channels. These structural features are consistent with the low specific surface area and weak intrinsic reactivity of stable crystalline minerals (Luo *et al.*, 2026). In contrast, raw rice husk powder (**Figure**

8(b)) displays a typical honeycomb-like porous biomass structure with wrinkled lamellar skeletons and rod-shaped siliceous components, which serves as a structural framework for particle loading and pore development during subsequent pyrolysis (Xiang *et al.*, 2026).

The uncalcined composite precursor (**Figure 8**(c) and (d)) shows only simple physical superposition of the two components. Rice husk lamellae partially adhere to nickel tailing aggregates without forming a stable integrated structure (Yang *et al.*, 2025). The compact surface lacks reconstructed pores and exposed active sites, resulting in limited Cr(VI) removal capacity (Mends *et al.*, 2025a).

After calcination at 600°C for 2 h under nitrogen atmosphere, the MNR composite undergoes marked structural rearrangement (**Figure 8**(e, f)). Dense nickel tailing particles are etched and refined, uniformly dispersed on the 3D porous biochar skeleton derived from rice husk pyrolysis with no obvious agglomeration (Huang *et al.*, 2025). This evolution is attributed to hierarchical pore generation from volatile release during carbonization, and particle fragmentation from lizardite dehydroxylation and phase transformation, consistent with XRD analysis. The modified MNR develops abundant interconnected hierarchical pores and nanoscale particles, with a specific surface area of 62.046 $m^2\ g^{-1}$, nearly 30 times that of raw biochar, in agreement with BET results.

The porous network improves accessibility of surface reactive sites (oxygen-containing functional groups and Fe(II) species confirmed by FTIR and XPS), providing sufficient interfacial sites for chromium retention. Meanwhile, interwoven rod-shaped siliceous fibers on the MNR surface stabilize the porous skeleton and physically confine $Cr(OH)_3$ precipitates within pores, limiting reoxidation and secondary migration of reduced Cr(III). The dispersed oxide particles on the biochar skeleton act as electron transfer mediators to accelerate bacteria-driven Fe(II)/Fe(III) redox cycling and promote Cr(VI) reduction (Xiang *et al.*, 2024).

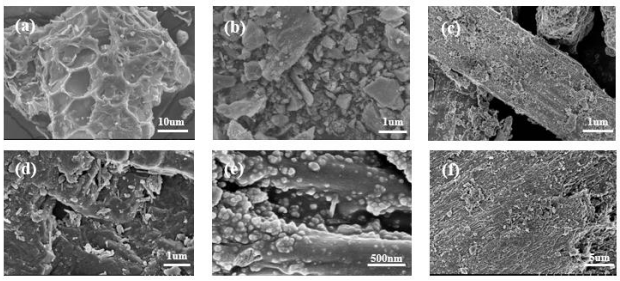

Figure 8. SEM images of (a) raw nickel tailings, (b) raw rice husk powder, (c, d) unmodified nickel tailings–rice husk powder mixture, and (e, f) modified MNR composite.

3.6. *Cr(VI) remediation experiments*

Solution physicochemical properties were determined at each sampling interval throughout the Cr(VI) removal experiments in simulated groundwater. The solution pH was measured at 0, 6, 12, 18, 24, 30, and 36 h using a calibrated benchtop pH meter (PHS-3C, LeiCi Instrument Co., Shanghai, China) equipped with a glass combination electrode. As shown in **Figure 9**, the solution pH increases gradually during the reaction, rising from an initial value of 7.42 ± 0.14 to 8.21 ± 0.03 at 36 h, and tends to stabilize after 30 h.

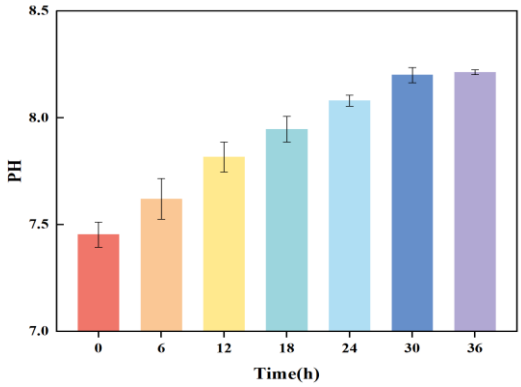

Figure 9. Temporal evolution of solution pH during Cr(VI) removal by the MNR–*Bacillus cereus* system. Data are mean ± standard deviation (n = 3).

Inductively coupled plasma mass spectrometry (ICP-MS) testing reveals that the concentration of dissolved Mg ions in the aqueous phase rises continuously and reaches a steady state after 30 h. As shown in **Figure 10**, dissolved Mg concentration increases from 0.42 ± 0.08 mg/L at 0 h to 9.31 ± 0.25 mg/L at 36 h. The consistent trends of Mg concentration and pH imply that Mg release from the MNR composite modulates solution alkalinity and drives the gradual pH elevation. Dissolution of Mg-bearing silicate phases (e.g., forsterite) in MNR releases Mg(II) into the aqueous phase, and the concomitant hydrolysis of silicate groups consumes protons, leading to the gradual pH increase.

Total dissolved Fe concentration was also monitored by ICP-MS. The results show that total dissolved Fe remains below 0.3 mg/L throughout the reaction. This low concentration is attributed to the weakly alkaline pH environment, which favors iron hydroxide precipitation. This indicates that homogeneous reduction by free dissolved Fe(II) in the aqueous phase is not a major Cr(VI) removal pathway.

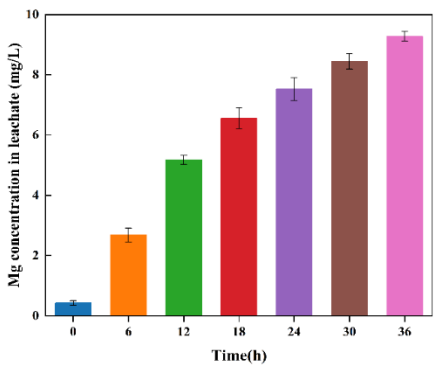

Figure 10. Temporal variation of dissolved Mg concentration in the leachate during Cr(VI) removal by the MNR–*Bacillus cereus* system. Data are mean ± standard deviation (n = 3).

Prior to spectrophotometric quantification of Cr(VI), a standard calibration curve was established under consistent DPC chromogenic reaction conditions (**Figure 11**), and all aqueous Cr(VI) concentrations were calculated

based on this curve. Blank correction was applied to all absorbance readings to eliminate matrix interference. Specifically, absorbance values of bacteria-containing groups were corrected using corresponding bacterial suspension blanks with identical inoculation ratios, while ultrapure water blanks were used for baseline calibration of bacteria-free samples. Moreover, control tests verified that the LB medium introduced via bacterial inoculation exerted negligible interference with Cr(VI) removal performance.

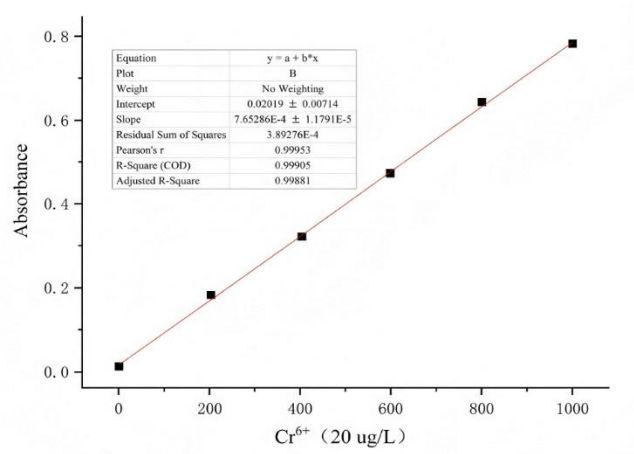

Figure 11. Standard calibration curve for Cr(VI) determined by DPC spectrophotometry at 540 nm.

Figure 12(a) presents the results for bacterial-coupled systems using MNR composites calcined at different temperatures, with all other experimental parameters kept constant. For all tested groups, Cr(VI) removal efficiency increases gradually with reaction time. At 6 h and 12 h, the 500°C-calcined MNR group exhibits the lowest removal capacity, while the 300°C and 400°C groups show comparable treatment performance. From 500°C to 700°C, removal efficiency generally increases with elevated calcination temperature. This temperature-dependent trend remains observable at 18 h and 24 h, with further improved Cr(VI) removal for all groups. At 30 h, the removal efficiency of all groups exceeds 84.06% ± 1.72%, and the performance discrepancy among different temperature groups gradually narrows. At 36 h, the 600°C group achieves a Cr(VI) removal efficiency of 97.25% ± 0.63%, while a further temperature increase to 700°C yields only marginal performance improvement. Based on comprehensive comparison of treatment effects, 600°C was selected as the optimal calcination temperature for MNR preparation in this study.

Figure 12(b) depicts the temporal changes in residual Cr(VI) content and removal efficiency at different MNR dosages in bacterial-inoculated systems (Qiu *et al.*, 2020). Consistent improvement in Cr(VI) removal is observed over time for all dosage groups, and higher MNR dosages correspond to better treatment performance throughout the reaction process. At 36 h, increasing the MNR dosage from 0.5 g to 1 g leads to a notable enhancement in Cr(VI) removal, whereas a further dosage increase to 2 g yields no obvious performance promotion. The group with 1 g MNR dosage reaches a removal efficiency of 99.81% ± 0.08% at 36 h, with no significant difference compared with the 2 g dosage group.

Figure 12(c) shows the Cr(VI) removal performance under different *Bacillus cereus* inoculation ratios. Overall, increased inoculum dosage corresponds to continuously improved Cr(VI) removal efficiency and faster reaction kinetics. Obvious performance enhancement is observed when the inoculation ratio increases from 1% (v/v) to 5% (v/v) at 12 h and 24 h. The 5% (v/v) group achieves a stable removal efficiency of 99.81% ± 0.06% starting from 18 h. At 36 h, the 2% (v/v) group also achieves nearly complete Cr(VI) removal, and the performance gap among high-concentration inoculation groups gradually diminishes at the later reaction stage.

Figure 12(d) presents the Cr(VI) removal results of bacteria-free systems with different nickel tailings-to-rice husk powder mass ratios. Pure nickel tailings display limited Cr(VI) removal capacity throughout the reaction. All composite groups exhibit better treatment performance than single-component groups (pure nickel tailings and pure rice husk powder). The composite group with a mass ratio of 1:2 maintains the optimal removal effect among all groups, with a removal rate of 58.67% ± 1.68% at 36 h. Compared with bacterial-coupled systems, all sterile groups show distinctly weaker Cr(VI) removal performance, implying the critical contribution of *Bacillus cereus* to chromium remediation (Guo *et al.*, 2021). Accordingly, the mass ratio of 1:2 was determined as the optimal raw material proportion for MNR precursor preparation.

To further quantify the individual contributions of each component and verify the nature of the interaction between MNR and *Bacillus cereus*, additional control groups were tested under optimal reaction conditions (600°C-calcined MNR, 1 g dosage, 5% (v/v) inoculation ratio, 1:2 raw material ratio, 18 h reaction), with all operational parameters fixed at constant levels. The results are summarized as follows:

(1) **Raw nickel tailings alone**: 1.02% ± 0.07% Cr(VI) removal;
(2) **Rice husk biochar alone**: 18.76% ± 0.45% Cr(VI) removal;
(3) **MNR alone** : 36.28% ± 0.84% Cr(VI) removal;
(4) ***Bacillus cereus* alone**: 52.53% ± 1.39% Cr(VI) reduction;
(5) **Full combined system (MNR + *Bacillus cereus*)**: 99.81% ± 0.06% Cr(VI) removal;
(6) **Abiotic control (heat-inactivated bacteria and blank matrix)**: < 0.5% Cr(VI) concentration change, negligible.

To quantitatively distinguish whether the enhanced performance of the combined system arises from a simple additive effect or a true synergistic interaction, the synergistic factor (SF) was employed as a quantitative indicator, defined as:

$$SF = \frac{\eta_{combined}}{\eta_{MNR} + \eta_{bacteria}} \quad (1)$$

where $\eta_{combined}$ is the Cr(VI) removal efficiency of the full combined system, η_{MNR} is the removal efficiency of MNR

alone, and $\eta_{bacteria}$ is the reduction efficiency of *Bacillus cereus* alone. An SF value greater than 1 indicates a synergistic effect between the two components, while SF = 1 and SF < 1 correspond to additive and antagonistic effects, respectively.

The calculated SF value under optimal conditions is approximately 1.12, well above the threshold of 1 for a synergistic effect. This result quantitatively confirms that the treatment performance of the combined system exceeds the expected additive effect of the two independent components, verifying the existence of a true synergistic effect rather than a simple superposition of individual functions. The synergistic effect can be attributed to the mutually promoting interaction between the two components: MNR provides a favorable microenvironment for bacterial colonization and metabolic activity, while the bacteria-driven Fe redox cycle in turn enhances the overall reductive conversion capacity of the system.

One-way analysis of variance (ANOVA) was performed to evaluate the effect of each factor on Cr(VI) removal efficiency (**Table 2**). The response variable was the mean removal efficiency across seven sampling points (0–36 h), with three independent replicates per level. All four factors showed significant effects ($p < 0.05$). Residual normality and variance homogeneity were tested. Welch ANOVA and Games–Howell tests were conducted as sensitivity analyses, confirming robust significance. Tukey honestly significant difference (HSD) was used for post-hoc painrwise comparisons. Note that F-values and effect sizes from separate single-factor experiments cannot be compared to rank factor influence. The results align with single-factor experimental trends, supporting the role of *Bacillus cereus* and the rationality of optimized parameters.

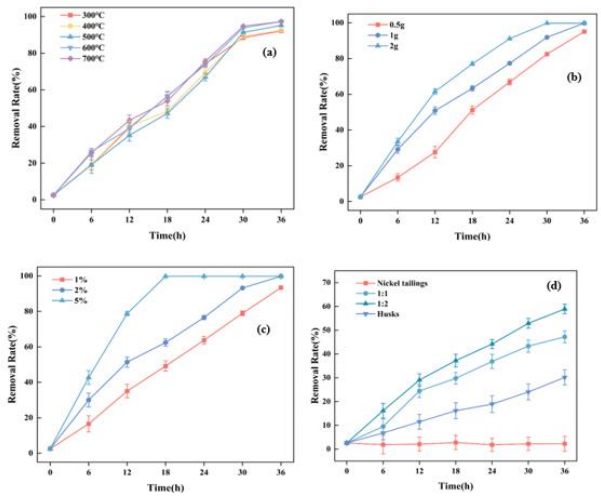

Figure 12. Residual Cr(VI) concentrations and removal efficiencies at different sampling time points across experimental groups. All systems except panel (d) were inoculated with *Bacillus cereus*. Variables for each panel: (a) calcination temperature of MNR material; (b) dosage of modified MNR material; (c) inoculum ratio of *Bacillus cereus*; (d) mass ratio of nickel tailings to rice husk powder, without *Bacillus cereus* inoculation. Data are mean ± standard deviation (n = 3).

Table 2. ANOVA results for factors affecting Cr(VI) removal efficiency.

Factor	df_1	df_2	F	p	η^2	ω^2
Temperature	4	10	12.8133	6.0118×10^{-4}	0.8367	0.7590
Bacterial suspension concentration	2	6	185.3580	4.0403×10^{-6}	0.9841	0.9762
Nickel-tailings/rice-husk powder ratio	3	8	133.2046	3.6227×10^{-7}	0.9804	0.9706
MNR mass	2	6	233.0025	2.0541×10^{-6}	0.9873	0.9810

3.7. *Chromium mass balance*

To quantitatively elucidate the fate of chromium in the synergistic remediation system, a chromium mass balance was established under optimal reaction conditions, with the initial total Cr(VI) mass in the simulated groundwater taken as 100%. The distribution of chromium across different phases is summarized in **Table 3**.

Solid-phase Cr speciation was quantified by anoxic acid extraction followed by FAS titration. Chromium retained in the solid phase is dominated by Cr(III), consistent with the reductive immobilization mechanism. The overall chromium recovery across the aqueous and solid phases reaches 98.91% ± 0.13%. The minor mass loss can be attributed to sample transfer losses during filtration and digestion. This mass balance confirms that the vast majority of Cr(VI) removed from the aqueous phase is successfully immobilized on the MNR solid matrix, providing quantitative support for the remediation performance of the synergistic system.

Table 3. Chromium mass balance of the MNR–*Bacillus cereus* synergistic system under optimal conditions.

Chromium fraction	Initial Cr (% of total)	Final Cr (% of total),	Percentage
Aqueous Cr(VI)	100	0.19 ± 0.06	0.19 ± 0.06
Aqueous Cr(III)	0	< 0.05	< 0.05
Solid-phase Cr(VI)	0	1.11 ± 0.04	1.11 ± 0.04
Solid-phase Cr(III)	0	97.61 ± 0.12	97.61 ± 0.12
Total recovered Cr	100	98.91 ± 0.13	98.91 ± 0.13

3.8. *Post-reaction Characterization of MNR Composite*

Post-reaction characterization was performed to clarify chromium immobilization pathways in the simulated groundwater system. ICP-OES confirmed total Cr accounted for 0.73% ± 0.01% of recovered MNR mass, consistent with theoretical calculations and verifying effective chromium enrichment on the solid matrix.

Valence titration showed dissolved Cr(III) in the final aqueous solution was below the detection limit, indicating nearly complete chromium transfer from the aqueous to solid phase. Further titration of anoxic acid-digested spent MNR verified dominant Cr(III) in the solid phase, directly confirming Cr(VI) reduction to Cr(III) during remediation.

Due to ultra-low chromium loading, high-resolution Cr 2p XPS spectra could not be clearly resolved, a common limitation for low-concentration heavy metal systems. Nevertheless, the detectable Cr signal in XPS survey spectra (**Figure 13**) corroborated chromium retention on the MNR surface.

Combined with the weakly alkaline microenvironment, SEM morphology and negligible LB medium interference, it is reasonably inferred that Cr(III) forms $Cr(OH)_3$ precipitates in situ, retained on the MNR surface and in pores via surface complexation and physical confinement by the siliceous fiber network. This inference aligns with stable chromium retention in batch experiments and supports long-term immobilization potential.

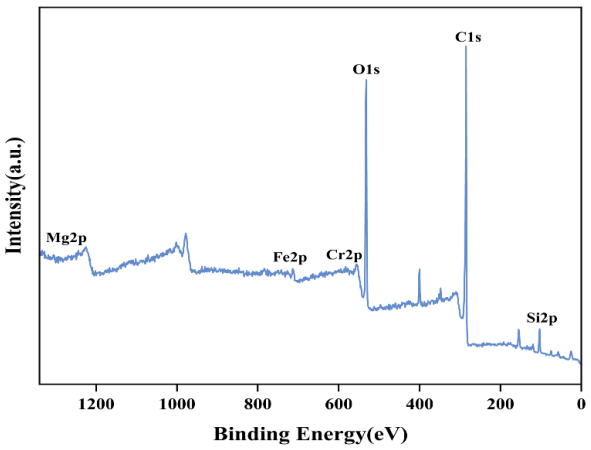

Figure 13. XPS survey spectrum of MNR composite after Cr(VI) remediation.

3.9. *Metal leaching and environmental safety*

To evaluate potential secondary contamination risks, dissolved metal concentrations in the aqueous phase were determined after remediation under optimal conditions. The dissolved Ni concentration was 0.04 ± 0.01 mg/L, well below widely accepted groundwater quality limits for nickel. Dissolved Fe concentration was 0.12 ± 0.02 mg/L, and total dissolved Cr was below 0.05 mg/L, both falling within safe thresholds for aquatic environments. No significant leaching of other major toxic heavy metals was detected beyond the quantified Ni, Fe and Cr species. The low leaching risk is attributed to the stable silicate crystalline phases of metal components in nickel tailings formed during high-temperature calcination, which are tightly bound to the biochar matrix and not easily released. Reduced Cr(III) mainly exists as $Cr(OH)_3$ precipitates confined within the pore structure, exhibiting low mobility. Chromium is stably immobilized in the solid phase of spent MNR materials with low leaching toxicity, posing negligible risk of secondary pollutant diffusion under natural environmental conditions, and the spent materials can be safely disposed of or potentially reused as auxiliary construction materials.

4. Discussion

Post-modification characterization confirms the MNR composite has favorable physicochemical properties for Cr(VI) removal. Hydration pretreatment and co-pyrolysis with rice husk biochar significantly increase its specific surface area, micropore volume and pore sites, and the interwoven siliceous porous framework formed during pyrolysis facilitates chromium capture (Jiang *et al.*, 2026). Modification induces in-situ conversion of lattice Fe(III) to Fe(II), as evidenced by shifts of C=C, Si-O, Mg-OH and Fe-O absorption peaks (Galani *et al.*, 2022). Surface Fe(II) sites donate electrons to reduce Cr(VI) upon contact, while abundant oxygen-containing functional groups and mineral bonds provide active sites for chromium retention. The mineral-carbon composite structure prevents pore collapse of pure biochar and exposes more mineral active sites (Zhao *et al.*, 2025).

Table 4 summarizes the key parameters and performance of representative Cr(VI) remediation systems from relevant studies (Mahajan *et al.*, 2025; Shao *et al.*, 2025; Hua *et al.*, 2025; Priyadarshini *et al.*, 2025), covering material type, microbial species, reaction conditions, treatment efficiency and remediation mechanism.

Most reported abiotic materials require acidic conditions to achieve high removal efficiency, and suffer from notable performance attenuation after repeated cyclic operation. Microbial systems usually require longer reaction times and exhibit lower treatment capacity for high-concentration pollution. In contrast, the MNR–*Bacillus cereus* coupled system accomplishes nearly complete Cr(VI) removal within a shorter reaction time under weakly alkaline conditions, and maintains stable remediation performance across multiple cycles. The unique microbe–iron cyclic coupling mechanism enables continuous regeneration of reductive Fe(II) sites, which is the core reason for its sustained high performance.

In simulated groundwater, the single MNR material achieves a maximum Cr(VI) removal efficiency of 58.74% within 36 h, whereas the MNR–*Bacillus cereus* coupled system attains complete Cr(VI) removal within 18 h. MNR gradually releases Mg(II) and Fe(II) ions, which buffer the solution pH within a stable range of 7.5–8.5 over the entire reaction process (Javed *et al.*, 2022). This weakly alkaline environment facilitates the reduction of soluble Cr(VI) to insoluble $Cr(OH)_3$ precipitates, thereby enabling stable immobilization of chromium in the aqueous phase (Giannakoudi *et al.*, 2025; Zheng *et al.*, 2021). *Bacillus cereus* exerts a synergistic effect with MNR to enhance the overall chromium removal performance (Nie *et al.*, 2023).

Based on all experimental and characterization results, a multi-process coupling mechanism of interfacial enrichment, microbial-iron synergistic reduction and chromium immobilization is proposed to explain the enhanced Cr(VI) removal by the synergistic system (**Figure 14**). The relative contributions of distinct removal pathways are clarified as follows.

Table 4. Comparison of Cr(VI) remediation performance between the MNR-*Bacillus cereus* system and representative materials from previous studies.

Adsorbent/ Material	Microorganism	Initial Cr(VI) concentration (mg/L)	Dosage	pH	Temperature (°C)	Reaction time (h)	Removal efficiency (%)	Mechanism
Microbial biomass system (Mahajan *et al.*, 2025)	Mixed microbial consortium	73.54	-	7.0	30-37	48.00	91.30%	Biosorption + extracellular chromate reductase reduction
Nano metal oxide material (Shao *et al.*, 2025)	None (abiotic)	100.00	0.5 g/L	Broad pH range	Room temperature	0.12	86.31%	Adsorption + ion exchange +complexation + reduction
Hydroxyapatite material (Priyadarshini *et al.*, 2025)	None (abiotic)	11.70	-	Neutral	Room temperature	3.00	100.00%	Electrostatic attraction + Fe (0) reductive precipitation
Mineral nanomaterial (Hua *et al.*, 2025)	None (abiotic)	100.00	0.7 g/L	7.0-9.6	Room temperature	168	100.00%	Bio-induced + bio-controlled mineralization
MNR-*Bacillus cereus* composite (This work)	*Bacillus cereus*	50.00	1.0 g	7.0-8.5	37	18.00	99.81 ± 0.06%	Microbial reduction and synergistic in-situ immobilization

First, the high specific surface area, hierarchical porous structure and abundant surface active groups of MNR enrich aqueous Cr(VI) at the solid-liquid interface via pore entrapment and surface complexation, providing ample sites for subsequent reduction. Meanwhile, forsterite dissolution in MNR releases Mg(II), sustaining a weakly alkaline microenvironment and driving gradual pH elevation, consistent with solution monitoring data. This condition supports bacterial metabolism and favors subsequent hydroxide precipitation of reduced chromium. In addition, trace structural Fe(II) leached from the mineral matrix remains surface-bound as the initial electron donor for the iron redox cycle. With total dissolved Fe below 0.3 mg/L throughout the reaction, homogeneous reduction by free aqueous Fe(II) is negligible, and iron-mediated redox proceeds predominantly at the solid-liquid interface.

Second, the *Bacillus cereus*-mediated coupled reduction pathway forms the core of efficient Cr(VI) removal, with cyclic iron regeneration as the key kinetic driver. This strain exhibits both Cr(VI) and Fe(III) reduction activities. Direct enzymatic reduction by bacteria contributes independently to Cr(VI) conversion, as verified by the bacteria-only control. Meanwhile, bacterial metabolism reduces surface-bound Fe(III) to Fe(II); the regenerated surface-associated Fe(II) acts as an efficient electron shuttle to rapidly reduce Cr(VI) to Cr(III) and is reoxidized to Fe(III) in turn, enabling sustainable iron cycling that accelerates electron transfer and reduction kinetics. Only trace iron participates in the cycle, avoiding excessive $Fe(OH)_3$ precipitation, consistent with dissolved Fe monitoring results (Pang *et al.*, 2024; Hu *et al.*, 2023).

Finally, valence speciation titration directly confirms Cr(VI) reduction to Cr(III), serving as solid experimental evidence for the reductive conversion. The reduced Cr(III) is thermodynamically prone to hydrolysis in the weakly alkaline environment to form amorphous $Cr(OH)_3$ phases, a reasonable inference supported by aqueous chromium chemistry and the extremely low dissolved total chromium in the reacted solution. The precipitated chromium species are retained on the MNR surface and in pores via surface complexation and physical confinement by the interwoven siliceous fiber network. Minor co-precipitation with Fe/Mg hydroxides also occurs but contributes marginally due to low dissolved metal ion concentrations. This immobilization pattern aligns with stable chromium retention in batch experiments and supports long-term chromium immobilization potential.

Compared with biochar- and mineral-based Cr(VI) remediation materials reported in existing literature (Li *et al.*, 2024; Rafiq *et al.*, 2023; Jiao *et al.*, 2023; Ramos *et al.*, 2024), the MNR–*Bacillus cereus* synergistic system possesses a unique microbe–iron cyclic coupling pathway. Conventional remediation materials predominantly rely on straightforward pollutant sequestration and lack a sustainable electron supply, whereas the self-regenerating iron electron donor within this system continuously drives Cr(VI) conversion, enabling stable chromium immobilization under laboratory conditions.

From an economic perspective, the MNR composite is synthesized entirely from two waste streams—nickel tailings (industrial solid waste) and rice husk (agricultural residue)—both of which incur negligible feedstock costs

while simultaneously achieving waste valorization. Its one-step low-temperature calcination synthesis route entails low energy consumption, with an estimated total production cost of approximately 120–150 USD per tonne, roughly 30–40% of the cost of commercial granular activated carbon for water treatment applications. This marked cost competitiveness gives the coupled system strong scalability potential for the large-scale in-situ remediation of Cr(VI)-contaminated groundwater.

Notably, this study is a laboratory proof-of-concept conducted using synthetic groundwater with a relatively high Cr(VI) concentration of 50 mg/L. This concentration was selected to fully characterize the reaction mechanism and evaluate the maximum treatment capacity of the system, but it is generally higher than Cr(VI) levels in most real contaminated groundwater, which typically range from sub-milligram per liter to several milligrams per liter. Differences in initial pollutant concentration may lead to variations in reaction kinetics and chromium immobilization pathways. In addition, synthetic groundwater has a simplified composition, whereas actual groundwater contains diverse coexisting ions and variable dissolved organic matter, both of which may compete for reactive sites or interfere with microbial metabolic activity and thus impair remediation performance. The experiments were also conducted at a constant 37°C optimized for *Bacillus cereus* metabolic activity, while natural groundwater typically ranges from 5 to 15°C, which may inhibit microbial activity and slow treatment kinetics. Targeted pilot-scale research employing a self-developed moving bed biofilm reactor (MBBR)-coupled system is currently underway to further evaluate the system's performance under more realistic groundwater conditions.

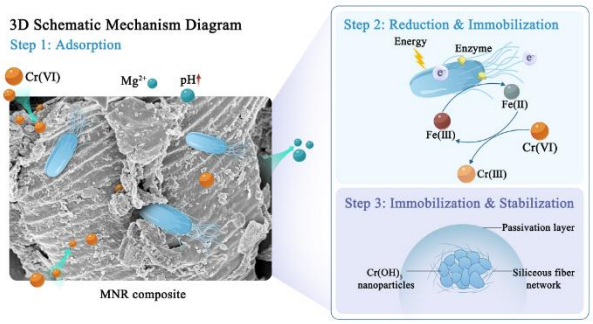

Figure 14. Mechanism diagram of Cr(VI) remediation by rice husk biochar-modified nickel tailings synergized with *Bacillus cereus* in simulated groundwater.

5. Conclusions

This study synthesized an MNR composite via rice husk modification of nickel tailings. The preparation parameters were optimized experimentally, with a nickel tailings-to-rice husk mass ratio of 1:2 and a calcination temperature of 600°C identified as the optimal conditions. The MNR–*Bacillus cereus* synergistic system was constructed and investigated for Cr(VI) removal performance. Under optimal conditions (1 g MNR dosage, 5% (v/v) bacterial inoculation), the system achieved 99.81% Cr(VI) removal within 18 h. The superior remediation performance arises from three synergistic pathways: interfacial enrichment of Cr(VI) on the MNR surface, Cr(VI) reduction via a bacteria-driven microbe-iron cyclic coupling mechanism, and enhanced microbial metabolic activity supported by the MNR framework. In addition, MNR maintains a weakly alkaline microenvironment favorable for bacterial metabolism, and converts highly mobile and toxic Cr(VI) into stable chromium hydroxide species with reduced aqueous bioavailability and long-term solid-phase immobilization potential. This work realizes the valorization of two types of waste streams. As a laboratory proof-of-concept study conducted with synthetic groundwater, further pilot-scale testing with real contaminated groundwater is required. Overall, the proposed synergistic system provides a promising strategy for the remediation of Cr(VI)-contaminated groundwater.

6. Acknowledgements

This work was financially supported by the National Key Research and Development Program of China [grant numbers:2022YFC3702300] and the National College Students' Innovation and Entrepreneurship Training Program (Grant No. 202511415030).

References

Chen, H. M., Zhang, J. W., Tang, L. Y., Su, M., Tian, D., Zhang, L., Li, Z., Hu, S. J. (2019), Enhanced Pb immobilization via the combination of biochar and phosphate solubilizing bacteria, Environment International, 127, 395-401.

Cheng, H., Zheng, X. Y., Zhu, Y., Wang, P., Zhu, J., Wei, J., Liu, Z. L., & Huang, C. (2024), Stabilization of sulfidated nano zerovalent iron with biochar: Enhanced transport and application for hexavalent chromium removal from water. Journal of Environmental Management, 371, 123045.

Choppala, G., Bolan, N., Kunhikrishnan, A., Bush, R. (2016), Differential effect of biochar upon reduction-induced mobility and bioavailability of arsenate and chromate, Chemosphere, 144, 374-381.

Galani, A., Mamais, D., Noutsopoulos, C., Anastopoulou, P., Varouxaki, A. (2022), Biotic and abiotic biostimulation for the reduction of hexavalent chromium in contaminated aquifers, Water, 14(1), 89.

Giannakoudi, M., Kokkinos, E., Tzamos, E., Zouboulis, A. (2025), Neutralization of Acid Mine Drainage using thermally treated chromite mining waste, Journal of Environmental Management, 387, 125936.

Greczynski, G., Hultman, L. (2020), X-ray photoelectron spectroscopy: Towards reliable binding energy referencing, Progress in Materials Science, 107.

Gu Y, Chen X, Liu L, Wang S, Yu X, Jia Z, Zhou X. (2023). Cr(VI)-bioremediation mechanism of a novel strain Bacillus paramycoides Cr6 with the powerful ability to remove Cr(VI) from contaminated water. J Hazard Mater. 455:131519.

Guo, S., Xiao, C., Zheng, Y., Li, Y., Chi, R. (2021), Removal and potential mechanisms of Cr(Ⅵ) contamination in phosphate mining wasteland by isolated Bacillus megatherium PMW-03, Journal of Cleaner Production, 322, 129062.

Hou, S., Du, J. K., Ling, H. B., Quan, S., Bao, J. G., & Yi, C. (2025), Synergistic Removal of Cr(VI) Utilizing Oxalated-Modified Zero-Valent Iron: Enhanced Electron Selectivity and Dynamic Fe(II) Regeneration. Nanomaterials, 15(9), 669.

Hu, S., Zhang, H., Yang, Y., Wang, W., Zhou, W., Shen, X., Liu, C. (2023), Reductive Sequestration of Cr(VI) and Immobilization

of C during the Microbially Mediated Transformation of Ferrihydrite-Cr(VI)-Fulvic Acid Coprecipitates, Environmental Science & Technology, 57, 8323-8334.

Hua, T.C., Li, Y.Z., Hu, Y.X., Yin, R.Z., Zhang, Y.N., Hou, B.X., Lu, H.Z., Ji, X., Bai, X.Z., Lu, A.H., Li, Y. (2025), Back to chromite as a mineralogical strategy for long-term chromium pollution control, Nature Communications, 16, 1975.

Huang, X., Tu, J., Wang, H., Xue, F., Zhao, X., Xiang, Y., Lan, J. (2025), Activated nickel tailings for remediation of arsenic-contaminated soils: Tailings activation, leaching toxicity and passivation mechanisms, Journal of Environmental Chemical Engineering, 13, 115912.

Irshad, M. A., Sattar, S., Nawaz, R., Al-Hussain, S. A., Rizwan, M., Bukhari, A., Waseem, M., Irfan, A., Inam, A., Zaki, M. E. A. (2023), Enhancing chromium removal and recovery from industrial wastewater using sustainable and efficient nanomaterial: A review, Ecotoxicology and Environmental Safety, 263, 115231.

Javed, K., Mahmood, S., Ammar, M., Abbas, N., Shah, M. Y., Ahmed, T., Mustafa, G. (2022), Rice husk ash adsorbent modified by iron oxide with excellent adsorption capacity for arsenic removal from water, International Journal of Environmental Science and Technology, 20, 2819-2828.

Jiang, M., Xu, Q., Hu, C. P., Song, J. Y., Liu, X. J., Yin, B., Xu, C. X., Liu, K., Ouyang, Z. Z. (2026), Mechanistic insights into Cr(vi) removal by acid-modified biochar via coupled redox and complexation processes, New Journal of Chemistry, 50(8), 3542–3554.

Jiao, Y., Xu, Q., Hu, Y., Wu, J., Su, X. (2023), Pyrolysis co-activation synthesized magnetic biochar for efficient removal of Cr(VI) from aqueous solution, Materials Chemistry and Physics, 295.

Kim, K. H., Kim, J.-Y., Cho, T.-S., Choi, J. W. (2012), Influence of pyrolysis temperature on physicochemical properties of biochar obtained from the fast pyrolysis of pitch pine (Pinus rigida), Bioresource Technology, 118, 158-162.

Li, H. S., Ishak, A. R., Aris, M. S. M., Shaifuddin, S. N. M., Ding, S., & Deng, T. T. (2025), Enhanced Removal of Hexavalent Chromium from Water by Nitrogen-Doped Wheat Straw Biochar Loaded with Nanoscale Zero-Valent Iron: Adsorption Characteristics and Mechanisms. Processes, 13(6), 1714.

Li, Z. H., Song, H. J., Zhang, X. Y., Hao, Y., Wu, A. R., Xu, S. L., Gao, R. X. (2024), Modification Strategies of Biochar and Their Research Progress in Cr(VI) Pollution Remediation, Chinese Journal of Analytical Chemistry, 52, 323–335.

Lin, Y.-W., Peng, S.-Y., Lee, W.-H., Lin, Y.-Y., Hung, M.-J., Lin, K.-L. (2023), Characterization of Cu^{2+} adsorption for eco-hydroxyapatite derived from limestone sludge via hydrothermal synthesis, Journal of Material Cycles and Waste Management, 25, 1069-1081.

Liu, B., Xin, Y.-N., Zou, J., Khoso, F. M., Liu, Y.-P., Jiang, X.-Y., Peng, S., Yu, J.-G. (2023), Removal of Chromium Species by Adsorption: Fundamental Principles, Newly Developed Adsorbents and Future Perspectives, Molecules, 28(2), 639.

Liu, H., Yao, R. L., Yu, M. L., Ye, Z. D., Lu, Y. R., Yu, X. L., Tang, J., Sun, J. T. (2025), Converting Waste into Treasure: Efficient Adsorption of Cr(VI) Using Iron-Modified Rice Straw Biochar, Toxics, 13(6), 458.

Liu, J.W., Sun, S., Zhang, H.X., Kong, Q., Li, Q., Yao, X.D. (2023), Remediation materials for the immobilization of hexavalent chromium in contaminated soil: Preparation, applications, and mechanisms, Environmental Research, 237, 116918.

Liu, L. H., Chen, Z. F., Yang, L. X., Yang, M. M., Wu, Q., Shi, M. X., Hou, B. (2023), Cage-like structured flexible hybrid fiber/SiO_2 aerogel composite for noise reduction, Ceramics International, 49, 31509-31516.

Liu, X., Zhang, L., Wang, Y., & Li, J. (2023), Removal of Chromium Species by Adsorption: Fundamental Principles, Newly Developed Adsorbents and Future Perspectives. Molecules, 28(2), 639.

Liu, Y., Liao, Y., Qiu, X., Qi, M., Liu, Z., Chen, H., Yang, W., Jiang, Z., He, C. (2025), A novel adsorbent for separation of Cr(VI) derived from abandoned amine-oxime resin by the hydrolysis method combined with extractant, Journal of Water Process Engineering, 71, 107377.

Lu, H. M., Liu, X. T., Dou, L. Z. (2015). Optimization of Growth Conditions for Bacillus cereus BC1 and BC2 [J]. Journal of Inner Mongolia Normal University (Natural Science Edition), 2015(5): 634-637. (in Chinese, with English abstract)

Luo, J., Liu, S., Sun, D., Mang, C., Rao, M., Li, G. (2026), Sustainable valorization of lateritic nickel tailings: Valuable metals recovery and gas-purifying materials fabrication, Results in Engineering, 29.

Mahajan, A., Singhal, P., Negi, S., Kumar, R., Jaswal, V.S., Ibrahim, A.A., Umar, A., Baskoutas, S. (2025), Microbial Strategies for the Removal of Hexavalent Chromium from Wastewater: Recent Advances and Future Prospects, Water, Air, & Soil Pollution, 236, 894.

Manoj, S., RamyaPriya, R., Elango, L. (2021), Long-term exposure to chromium contaminated waters and the associated human health risk in a highly contaminated industrialised region, Environmental Science and Pollution Research, 28, 4276-4288.

Mends, E. A., Arthur, S. E., Hussaini, S., Thella, J. S., Chu, P. (2025b), Investigating the selective extraction of metals from nickel sulfide tailings using salt roasting and acid leaching, Minerals Engineering, 231.

Mends, E. A., Arthur, S. E., Tita, A. M., Hussaini, S., Osho, B., Timilsina, A., Basyal, S., Yang, Y., Chu, P. (2025a), Leaching nickel sulfide tailings with activated carbon in sulfuric acid medium, Separation and Purification Technology, 353, 128520.

Meyers, A., Furtmann, C., Jose, J. (2018). Direct optical density determination of bacterial cultures in microplates for high-throughput screening applications. Enzyme and Microbial Technology, 118, 1-5.

Mondal, G., Sahoo, P., Banerjee, S., Nandi, R., Ghosh, C., Mandal, J., Bhattacharyya, P. (2025), Utilizing nano zero-valent iron impregnated biochar for removal of hexavalent chromium from water: An assessment through Box-Behnken optimization, kinetics, and isotherm studies, Groundwater for Sustainable Development, 29, 101446.

Nie, M., Cai, M., Wu, C., Li, S., Chen, S., Shi, G., Wang, X., Hu, C., Xie, J., Tang, Y., Zhang, H., Zhao, X. (2023), Selenium-mediated Cr(VI) reduction and SeNPs synthesis accelerated Bacillus cereus SES to remediate Cr contamination, Journal of Hazardous Materials, 457, 131713.

Pang, A., Zhang, S., Zhang, X., Liu, H. (2024), Mechanism of Cr(VI) bioreduction by Clostridium sp. LQ25 under Fe(III) reducing conditions, Chemosphere, 350, 141099.

Prajapati, J., Badola, A., Bhoi, B., Chandra, V. (2026), Efficient removal of hexavalent chromium from water using $MnFe_2O_4$ encapsulated polyaniline nanocomposite, Materials Science and Engineering B, 323, 118741.

Priyadarshini, N., Ilaiyaraja, P., Prartthana, M.P., Pragateesh, K.D., Akshaya, S.B. (2025), Mini review on hydroxyapatite based adsorbents for hexavalent chromium removal: recent advances and Indian relevance, Proceedings of the Indian National Science Academy.

Qiao, H. Y., Hu, J., & Zhao, Y. S. (2024). Study of the nano zero-valent iron stabilized by carboxymethyl cellulose loaded on biochar for remediation of Cr(VI)-contaminated groundwater. Separation and Purification Technology, 353, 128494.

Qiu, Y., Zhang, Q., Gao, B., Li, M., Fan, Z., Sang, W., Hao, H., Wei, X. (2020), Removal mechanisms of Cr(VI) and Cr(III) by biochar supported nanosized zero-valent iron: Synergy of adsorption, reduction and transformation, Environmental Pollution, 265, 115018.

Radfarnia, H., Staneva, K., Shafeen, A., Zanganeh, K., Patarachao, B., Huertas, S. V., Zborowski, A., Kung, J., Kenari, S. L. D., Mosadeghsedghi, S., Volchek, K. (2025), Experimental Study on Indirect CO_2 Mineralization of Industrial Solid Wastes: Electric Arc Furnace (EAF) Slag and Nickel Mine Tailings, ACS Omega, 10, 41571-41585.

Rafiq, S., Wongrod, S., Vinitnantharat, S. (2023), Adsorption Kinetics of Cadmium and Lead by Biochars in Single- and Bisolute Brackish Water Systems, ACS Omega, 8, 45262-45276.

Ramos, R. L., Faria, D. B., Maronezi, V., de Campos, V., Furquim, S. A. C., Shinzato, M. C. (2024), Comparative study of hexavalent chromium removal by oxisol and synthesized iron minerals, Environmental Earth Sciences, 83.

Rowe, H., Hughes, N., Robinson, K. (2012), The quantification and application of handheld energy-dispersive x-ray fluorescence (ED-XRF) in mudrock chemostratigraphy and geochemistry, Chemical Geology, 324–325, 122–131.

Schneider, J., Lunghi, E., Waldvogel, S. R. (2025), Electrochemical Dehydration Reaction, ChemSusChem, 18, e202501552.

Shao, T.W., Yin, Q., Bai, J.Y., Zhu, J.Y., Gan, M. (2025), Adsorption and catalytic reduction of nanomaterials: A review on metal, metallic oxide, metallic sulfide and carbon-based catalyst, Environmental Research, 266, 120449.

Shi, C. Z., Hu, R. R., Zhou, H. B., Bie, X. M., & Yang, J. (2026). Establishing a Rapid Enrichment Medium for *Bacillus cereus* to Shorten Detection Time. Foods, 15(3), 466.

Sinha, R., Kumar, R., Sharma, P., Kant, N., Shang, J. Y., Aminabhavi, T. M. (2022), Removal of hexavalent chromium via biochar-based adsorbents: State-of-the-art, challenges, and future perspectives, Journal of Environmental Management, 317, 115356.

Tripathi, M., Pathak, S., Singh, R., Singh, P., Singh, P. K., Shukla, A. K., Maurya, S., Kaur, S., Thakur, B. (2024), A Comprehensive Review of Lab-Scale Studies on Removing Hexavalent Chromium from Aqueous Solutions by Using Unmodified and Modified Waste Biomass as Adsorbents, Toxics, 12(9), 657.

Trittschack, R., Grobéty, B., Koch-Müller, M. (2012), In situ high-temperature Raman and FTIR spectroscopy of the phase transformation of lizardite, American Mineralogist, 97, 1965–1976.

Wang, H. F., Guo, J., Chen, X., & He, H. X. (2023). The Metabolomics Changes in Luria–Bertani Broth Medium under Different Sterilization Methods and Their Effects on Bacillus Growth. Metabolites, 13(8), 948.

Wang, H., Li, S., Zhou, Y., & Zhang, M. (2024), Iron-assisted microbial reduction of Cr(VI) by Bacillus cereus: Kinetics and electron shuttle mechanism. Journal of Hazardous Materials, 463, 132987.

Wu, X., Li, S., Li, M. (2018), Effect of temperature on the properties of charcoal prepared from carbonization of biorefinery lignin, BioResources, 13, 6736-6745.

Xiang, Y., Huang, X., Wang, H., Lan, J., Hou, H. (2026), Nickel tailings-derived precursors for Fe-Ni-Ti@SiO_2 synthesis: Multicomponent microcosmic reactions, environmental catalysis, and regeneration high-value, Process Safety and Environmental Protection, 206.

Xiang, Y., Lan, J., Cai, Y., Dong, Y., Hou, H. (2024), Modified nickel–cobalt tailing activated PMS for highly efficient degradation of organic pollutants: Multiple-scale effect and active sites, Chemical Engineering Journal, 482, 149196.

Xiong, L., Hu, H. S., Liu, M. T., & Li, X. Y. (2025), Fly ash-doped biochar-supported nZVI composite for Cr(VI) removal: Synthesis, performance, and mechanism. Colloids and Surfaces A: Physicochemical and Engineering Aspects, 724, 137521.

Xu, L., Xu, Z., Zhang, F., Yuan, Y., Cheng, B., Zhang, C., Chen, P., Huang, X., Lin, Y., Gu, M. (2022), Experimental Study on Pyrolysis of Rice Straw Catalyzed by CaO/Al_2O_3-Phosphate Mixture, BioEnergy Research, 15, 2006-2025.

Yang, D. X., Liu, T., Deng, R. Y., Xian, Z. H., Chen, Y. (2024), Porous biochar-driven innovative Cr(VI) reduction and resource recovery, Chemical Engineering Journal, 499, 156556.

Yang, J., Wang, X., Shen, B., Hu, Z., Xu, L., Yang, S. (2020), Lignin from energy plant (Arundo donax): Pyrolysis kinetics, mechanism and pathway evaluation, Renewable Energy, 161, 963-971.

Yang, X., Gao, L., Wu, Y., Chen, Y., Tong, L. (2022), Extraction of Magnesium and Nickel from Nickel-Rich Serpentine with Sulfation Roasting and Water Leaching, Metals, 12.

Yang, Z., Gu, H., Liu, S., Wu, K., Xu, L., Guo, L. (2025), Insights into the dissolution kinetics of copper–nickel tailings for CO_2 mineral sequestration, International Journal of Minerals, Metallurgy and Materials, 32, 2119–2130.

Zhang, Q., Wu, S., Zhao, L., & Sun, W. (2023), Scalable production of waste-derived biochar composites for groundwater remediation: Techno-economic analysis. Journal of Cleaner Production, 413, 137529.

Zhang, W., Xue, Z., Zou, Z., Saxén, H. (2022), The Ideal and Regular Mechanisms of Hematite Reduction Reactions, Crystal Research and Technology, 5.

Zhao, T., Li, G., Zhang, S., Yang, H., Ni, W., Shao, A. (2025), Enhancement effect of biochar on the immobilization of heavy metals and anions in MSWI fly ash/bottom ash–coal fly ash-based cementitious materials: Risk assessment model and mechanisms, Journal of Hazardous Materials, 497, 139615.

Zheng, C., Yang, Z., Si, M., Zhu, F., Yang, W., Zhao, F., Shi, Y. (2021), Application of biochars in the remediation of chromium contamination: Fabrication, mechanisms, and interfering species, Journal of Hazardous Materials, 407, 124376.

Zheng, N., Zhou, Q., Wang, R., Lian, Y., He, X., Hu, R., Hu, Z. (2022), Rust triggers rapid reduction of Cr^{6+} by red phosphorus: The importance of electronic transfer medium of Fe^{3+}, Chemosphere, 303, 134971.